

# A Photorealistic Dataset and Vision-Based Algorithm for Anomaly Detection During Proximity Operations in Lunar Orbit

Selina Leveugle<sup>1</sup>, Chang Won Lee<sup>2</sup>, Svetlana Stolpner<sup>3</sup>, Chris Langley<sup>3</sup>,  
Paul Grouchy<sup>3</sup>, Steven Waslander<sup>2</sup>, and Jonathan Kelly<sup>1</sup>

**Abstract**—NASA’s forthcoming Lunar Gateway space station, which will be uncrewed most of the time, will need to operate with an unprecedented level of autonomy. One key challenge is enabling the Canadarm3, the Gateway’s external robotic system, to detect hazards in its environment using its onboard inspection cameras. This task is complicated by the extreme and variable lighting conditions in space. In this paper, we introduce the visual anomaly detection and localization task for the space domain and establish a benchmark based on a synthetic dataset called ALLO (Anomaly Localization in Lunar Orbit). We show that state-of-the-art visual anomaly detection methods often fail in the space domain, motivating the need for new approaches. To address this, we propose MRAD (Model Reference Anomaly Detection), a statistical algorithm that leverages the known pose of the Canadarm3 and a CAD model of the Gateway to generate reference images of the expected scene appearance. Anomalies are then identified as deviations from this model-generated reference. On the ALLO dataset, MRAD surpasses state-of-the-art anomaly detection algorithms, achieving an AP score of 62.1% at the pixel level and an AUROC score of 74.9% at the image level. Given the low tolerance for risk in space operations and the lack of domain-specific data, we emphasize the need for novel, robust, and accurate anomaly detection methods to handle the challenging visual conditions found in lunar orbit and beyond.

## I. INTRODUCTION

Over the past two decades, the international space community has begun to focus its efforts on extending human space exploration beyond low-Earth orbit. NASA’s Artemis program aims to deploy the Lunar Gateway, the first space station in lunar orbit, that will test new technologies needed for extended deep-space missions [1]. Unlike the International Space Station (ISS), the Gateway will be required to operate autonomously and without an on-board crew for long periods. Complete autonomy is advantageous for the Canadarm3, the external robotic system being developed by MDA Space for the Canadian Space Agency. It will play a multifaceted role on the Gateway, including station maintenance, inspection, and capture and berthing of visiting vehicles [2].

<sup>1</sup>Space and Terrestrial Autonomous Robotic Systems (STARS) Laboratory, University of Toronto Institute for Aerospace Studies (UTIAS), Toronto, Ontario, Canada. Email: <firstname>.<lastname>@robotics.utias.utoronto.ca.

<sup>2</sup>Toronto Robotics and AI Laboratory (TRAIL), University of Toronto Institute for Aerospace Studies (UTIAS), Toronto, Ontario, Canada. Email: john.lee@robotics.utias.utoronto.ca; steven.waslander@robotics.utias.utoronto.ca.

<sup>3</sup>MDA Space Inc. Email: <firstname>.<lastname>@mda.space.

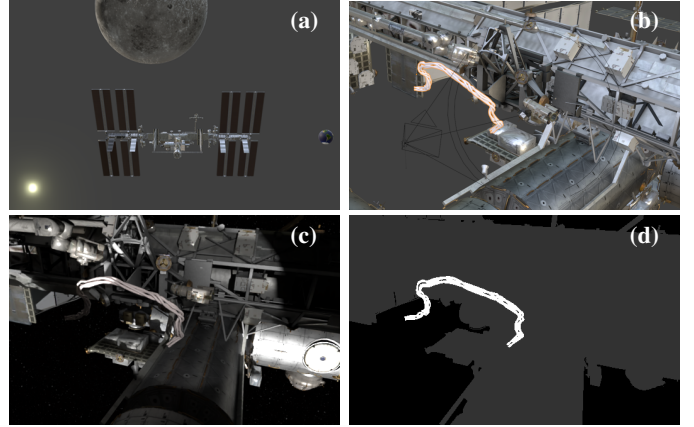


Fig. 1: Visualization of the rendering process used to generate an anomalous image in the ALLO dataset. (a) Positions of the Sun, Moon, and space station are determined and scene lighting is configured accordingly; (b) An anomaly is inserted into the scene; (c) The Blender Cycles engine renders the image; and (d) the corresponding three-class segmentation mask is generated.

To enhance robotic autonomy, vision-based anomaly detection methods that can autonomously detect collision hazards, such as loose tools or debris, are of particular interest. Anomaly detection and localization involve identifying and pinpointing the locations of unexpected content in images that deviate from a set of expected inputs. Anomaly detection in the space domain is particularly challenging because of complex lighting conditions that result from the black background coupled with harsh direct solar illumination. Furthermore, the varied camera viewpoints used during operations near the space station can cause anomalies to fall into the shadow of the station and blend in with the background, making detection substantially more difficult.

Although reliable automated anomaly detection would be highly valuable, existing datasets and methods do not directly address the problem of anomaly detection in the space domain. Specifically, a significant challenge in space anomaly detection is the absence of comprehensive, labelled datasets necessary for robust evaluation. Moreover, our comparative analysis demonstrates that existing approaches significantly underperform and fail to generalize effectively to this domain. To address these gaps, we introduce ALLO, a large-scale open-source anomaly detection dataset tailored for robotic proximity operations in space. Using ALLO, we establish a new benchmark by evaluating existing anomaly detection

algorithms. In addition, we present MRAD, a novel, statistical algorithm specifically designed for this application. MRAD leverages camera pose information and a known CAD model of the station to perform per-image anomaly detection, achieving state-of-the-art performance on the ALLO benchmark. In summary, our main contributions are as follows:

- we introduce ALLO, a synthetic dataset for vision-based anomaly detection in the space domain, and release its open-source generation pipeline to facilitate extensions and future research;
- we establish a new anomaly detection benchmark using ALLO, evaluating recent anomaly detection algorithms and highlighting their shortcomings for the space environment;
- we introduce Model Reference Anomaly Detection (MRAD), a statistical algorithm specifically designed for the space domain, and demonstrate its superior performance over existing anomaly detection algorithms on ALLO through comprehensive evaluation and ablation studies.

The remainder of this paper is structured as follows. In Section II, we review existing anomaly detection datasets and algorithms. In Section III, we detail the ALLO dataset and its rendering pipeline. We then describe our proposed MRAD algorithm in Section IV and evaluate its performance against other state-of-the-art methods on the ALLO dataset in Section V. The ALLO dataset and all open-source code are available from the anonymous repository at <https://anonymous.4open.science/r/ALLO-00A8>.

## II. RELATED WORK

Although anomaly detection is an emerging topic in the space domain, there is extensive work on visual datasets for space applications and, separately, on industrial anomaly detection. In this section, we review existing image datasets for these two applications. In addition, we provide an overview of modern anomaly detection methods which will serve as baselines for our benchmark.

### A. Datasets for Space Applications and Defect Inspection

1) *Space Applications*: Synthetic visual datasets are widely used in space applications due to the difficulty of acquiring real in situ imagery. Photorealistic rendering engines such as the Blender Cycles [3] engine and Unreal Engine 5 [4] are commonly employed to produce simulated space imagery. Existing datasets typically focus on specific mission scenarios. For instance, Airbus’s SurRender [5] generates images for satellite servicing and debris removal, while the Space Imaging Simulator for Proximity Operations (SISPO) [6] leverages Blender to model asteroid fly-bys.

Physical simulators have also been developed. Legentil et al. [7], for example, capture docking-port imagery under realistic dynamics and challenging lighting conditions to support satellite rendezvous and docking operations. Their dataset explicitly excludes the satellite body to ensure satellite-agnostic applicability for docking-port detection and state estimation.

In contrast, the ALLO dataset provides a comprehensive photorealistic simulation of an entire space station in lunar orbit, specifically designed for anomaly detection to mitigate collision risks. Its open-source data-generation pipeline further enables adaptation to diverse downstream tasks.

2) *Industrial Defect Inspection*: The majority of recent efforts in anomaly detection have focused on finding manufacturing defects during visual industrial inspection. The MVTec 2D anomaly detection dataset [8] is the most widely used benchmark for this application due to its pixel-level annotations and diverse range of objects and textures [9]. However, similar to other anomaly detection datasets such as BTech [10] and Kolektor [11], MVTec images are all captured from the same perspective, under consistent lighting and with simple backgrounds. In contrast, the ALLO dataset offers a more comprehensive and diverse set of scenes, including multiple views of the ISS with varied lighting conditions and backgrounds.

### B. Anomaly Detection Methods

Anomaly detection involves identifying abnormal samples, such as unexpected or irregular instances, that deviate from an expected distribution. Existing methods fall broadly into two categories: statistical approaches, which rely on (possibly learned) statistical models, and deep learning-based approaches, which use deep neural networks to learn a representation of normal (non-anomalous) data.

1) *Statistical Detectors*: Statistical detection methods compute anomaly scores using distance functions or statistical tests, followed by binary classification via empirical thresholds or probabilistic models [12]. Classical techniques such as one-class support vector machines (OC-SVM) [13] and support vector data descriptors (SVDD) [14] model the density or decision boundary of normal data to identify outliers. The Reed–Xiaoli detector (RXD) [15], originally developed for use with hyperspectral aerial imagery, assumes a multivariate Gaussian distribution for background pixels and detects anomalies as probabilistic outliers. However, this assumption fails for complex, non-homogeneous scenes such as those encountered in space.

Several RXD extensions relax its homogeneity requirement. The probabilistic anomaly detector (PAD) [16] separates pixels into target and background sets and compares their RXD scores, while the random selection-based anomaly detector (RSAD) [17] iteratively redefines the background set to improve robustness. Nevertheless, these methods remain sensitive to background variability and are not designed to exploit geometric priors available in space applications.

2) *Deep Learning-Based Detectors*: Most of the modern deep learning-based anomaly detectors are unsupervised due to the scarcity of labelled anomalies, although some self-supervised approaches introduce synthetic anomalies during training [18], [19]. Unsupervised methods [20]–[22] learn a representation of normal data and detect deviations at inference time. Many operate in feature space, using pre-trained backbones (e.g., ResNet) and either fit statistical models to extracted features [20], [22] or estimate their density with

normalizing flows [23], [24]. Alternatively, generative approaches reconstruct only normal images, flagging anomalies by their reconstruction error [9]. Student–teacher architectures [21], [25] follow this paradigm by distilling normal data representations from a teacher to a student, which fails to reproduce unseen anomalous patterns.

Although these methods achieve state-of-the-art results in structured domains such as industrial defect detection, they generalize poorly to the space domain due to high scene variability, complex lighting, and limited representative training data for learning.

### III. THE ALLO PIPELINE AND DATASET

Our first contribution is a dataset for space-based anomaly detection and localization. The ALLO dataset comprises 51,409 synthetic images simulating the visual feed from arm-mounted cameras. The dataset is divided into a training set of normal (anomaly-free) images and a test set containing both normal and anomalous examples. Each image is generated with the Blender Cycles path-tracing engine, realistically simulating the lighting conditions in lunar orbit, including the blackness of deep space, direct sunlight, and inspection lighting. The image-generation pipeline, described below, is fully open source and can be adapted for related computer vision tasks, such as semantic segmentation and depth estimation.

#### A. Scene Modelling

We use a high-fidelity Blender model of the ISS [26] as a stand-in for the Lunar Gateway, as no detailed Gateway model is currently available. Given the expected architectural and surface similarities of the Gateway to the ISS, this model provides a realistic approximation of the visual environment anticipated for the Canadarm3’s operations. The Gateway’s anticipated orbit [27] is approximated by an ellipse matching the expected perilune and apolune.

The positions of the Earth and Sun are determined over a 365-day period relative to the Moon using 2030 ephemeris data from the Skyfield library [28]. These bodies are positioned relative to the ISS model to replicate the background views expected by the arm’s cameras. For computational efficiency, all models are scaled down in size but positioned to preserve their apparent angular sizes from the station’s perspective, ensuring visual fidelity.

To simulate the arm-mounted camera perspectives, 50 unique base poses are manually defined around the ISS. To introduce realistic pose imprecision and enhance viewpoint diversity, each base pose is perturbed with Gaussian noise during rendering, using standard deviations of 1 m for position and 0.2 rad for orientation (roll, pitch, and yaw). This randomization strategy ensures comprehensive coverage of the relevant station regions and subtle yet critical variations in perspective.

#### B. Image Rendering

Different camera positions are used for the training and test sets to avoid viewpoint overlap. The test set contains

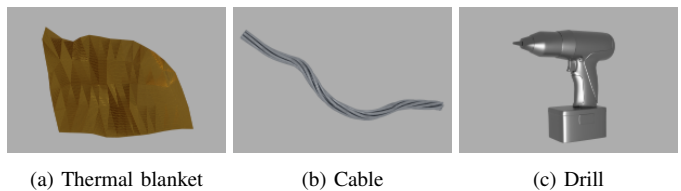


Fig. 2: Examples of models of anomalous objects used in the ALLO dataset.

16 distinct anomalous objects representing potential hazards, including dislodged station equipment or items lost during extravehicular activities (e.g., thermal blankets, cables, tools), as well as objects resembling small experimental satellites from prior missions (Fig. 2).

For each anomalous scene, only one such object is inserted into the camera’s view frustum to simplify evaluation. The object is randomly positioned within the station’s vicinity and rendered at five depths: one initial random depth and additional positions displaced by  $\pm 1$  m and  $\pm 2$  m from this initial position. If the object is occluded or projected to occupy less than 0.1% of the image, it is repositioned to ensure visibility. This procedure yields a diverse set of anomaly appearances while maintaining realistic spatial consistency.

Each rendered image has a resolution of  $1,920 \times 1,080$  pixels and is paired with a three-class segmentation mask delineating the background, non-anomalous foreground (e.g., station surfaces, celestial bodies), and anomalous regions. The rendering pipeline, illustrated in Fig. 1, is repeated with two random seeds to expand the dataset. The dataset composition is reported in Table I, with sample images shown in Fig. 3.

In summary, scenes were generated for each day in the ephemeris data by first positioning the Moon, Earth, and Sun according to their ephemerides. Camera poses were then selected, with indices 0–39 assigned to normal scenes and 40–49 reserved for anomalous ones. For each camera pose and anomaly configuration, the following steps were executed:

- 1) Place the camera with a Gaussian pose perturbation.
- 2) Add a nearby spotlight.
- 3) If the scene is anomalous:
  - 3.1) Insert the anomaly into the view frustum.
  - 3.2) Reposition the anomaly for visibility if necessary.
- 4) Add noise and glare.
- 5) Render the image and corresponding segmentation mask using the Blender Cycles engine.

#### C. Image Validation

To validate the realism of our synthetic ALLO images, we compared them with real photographs of the ISS from past ISS missions. We matched Blender camera poses to these reference images, ensuring precise geometric alignment, producing synthetic renderings that closely replicate real lighting conditions and surface textures (see Fig. 4).

Quantitatively, we used the learned perceptual image patch similarity metric (LPIPS) [29] across ten real–synthetic pairs, obtaining an average score of 0.58—comparable to state-of-the-art image synthesis models such as GILL ( $\sim 0.70$  on VIST) [30] and Stable Diffusion XL (0.88 on COCO2017) [31].

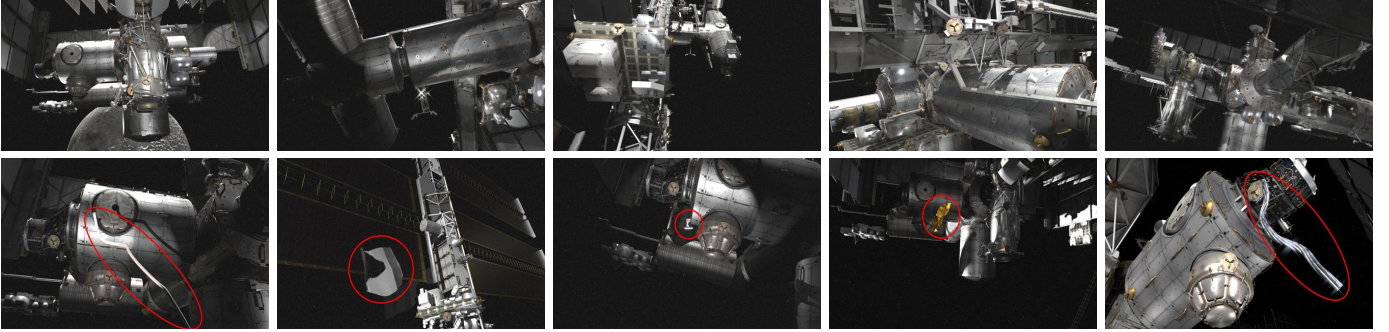


Fig. 3: Sample images from the ALLO dataset. *Top Row*: Normal (anomaly-free) images captured from five distinct camera views of the ISS. *Bottom Row*: Images containing anomalies, identified by red ellipses, that include free-floating equipment such as cables, thermal blankets, and a hand drill.

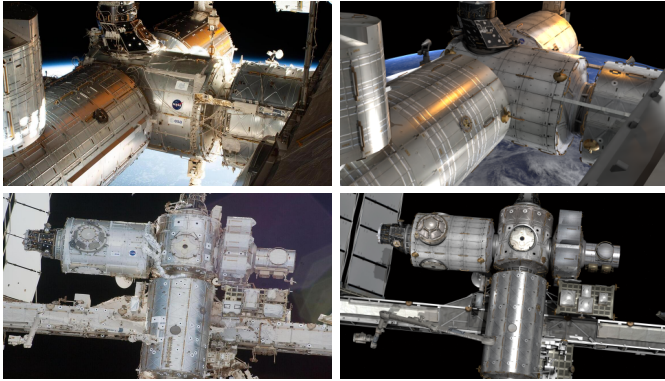


Fig. 4: Real images of the ISS (left) and their synthetic recreations (right).

We also calculated the Fréchet inception distance (FID) [32] between 319 ALLO training images and historical ISS photographs, achieving a score of 3.61. This FID score surpasses those of other recent models, such as DiGIT [33] (4.59 on ImageNet) and LC-GAN [34] (5.77 on AFHQ-v2). Together, these two metrics confirm the high quality and photorealism of our synthetic images.

Together, these qualitative and quantitative results confirm that the synthetic images effectively reproduce the visual characteristics of the target space environment.

#### IV. MODEL REFERENCE ANOMALY DETECTION

MRAD is an anomaly detection algorithm tailored for the space domain. It detects anomalies by comparing a query image with a reference image rendered from a known camera pose and a CAD model. The algorithm operates in three stages: (1) pixel-level anomaly scores are computed using an extended version of the Reed–Xiaoli detector (RXD) applied to query–reference pairs; (2) region growing is used to cluster pixels into candidate anomalous regions, producing a binary

TABLE I: Composition of the ALLO dataset (camera poses and images) across the training and test sets. The training set is composed exclusively of normal images, while the test set contains both normal and anomalous images rendered from disjoint sets of camera poses.

Dataset Set	Training	Test	Total
Camera Poses	1–40	41–50	50
Normal Images	29,085	7,300	36,385
Anomalous Images	0	15,024	15,024

mask; and (3) an image is classified as anomalous if the total detected area exceeds a threshold. In our work, both reference and query images are synthetically generated—we simulate the domain gap between real and synthetic data by introducing random variations in lighting and pose when rendering the reference images.

##### A. Reed–Xiaoli Detector (RXD) Anomaly Score

Each pixel in the query image is first assigned an anomaly score based on the Reed–Xiaoli detector (RXD) [15], which measures a pixel’s statistical distance from the background. RXD models nominal pixels as samples from a multivariate Gaussian distribution with mean vector  $\boldsymbol{\mu} \in \mathbb{R}^3$  and covariance matrix  $\boldsymbol{\Sigma} \in \mathbb{R}^{3 \times 3}$ . Pixels with low likelihood under  $\mathcal{N}(\boldsymbol{\mu}, \boldsymbol{\Sigma})$  are considered anomalous. Given an image  $I$  with mean  $\boldsymbol{\mu}_I$  and covariance  $\boldsymbol{\Sigma}_I$ , the RXD anomaly score for a pixel  $\mathbf{x}$  is the squared Mahalanobis distance:

$$\text{RXD}_I(\mathbf{x}) = (\mathbf{x} - \boldsymbol{\mu}_I)^T \boldsymbol{\Sigma}_I^{-1} (\mathbf{x} - \boldsymbol{\mu}_I). \quad (1)$$

While effective for relatively homogeneous scenes, RXD struggles with non-uniform backgrounds, such as space imagery, where lighting and texture vary significantly. To address this limitation, we adapt principles from the probabilistic anomaly detector (PAD) [16], which compares likelihoods under both nominal and anomalous distributions. In MRAD, the nominal (anomaly-free) distribution is derived directly from the reference image, while the query image provides statistics for potentially anomalous regions. Specifically, the anomaly-free distribution statistics  $(\boldsymbol{\mu}_0, \boldsymbol{\Sigma}_0)$  are computed from the reference image, and the query distribution statistics  $(\boldsymbol{\mu}_1, \boldsymbol{\Sigma}_1)$  are computed from the query image. The MRAD anomaly score for a pixel  $\mathbf{x}$  is then defined as

$$\text{MRAD}(\mathbf{x}) = \text{RXD}_{\text{ref}}(\mathbf{x}; \boldsymbol{\mu}_0, \boldsymbol{\Sigma}_0) - \text{RXD}_{\text{query}}(\mathbf{x}; \boldsymbol{\mu}_1, \boldsymbol{\Sigma}_1), \quad (2)$$

where, given nominal image alignment,  $\text{RXD}_{\text{ref}}(\mathbf{x})$  is expected to be greater than or equal to  $\text{RXD}_{\text{query}}(\mathbf{x})$ .

To account for spatial variability in lighting and texture (e.g., the contrast between the black background of space and the station’s surface), both reference and query images are divided into  $4 \times 4$  grids. Mean and covariance statistics are computed per grid, yielding localized anomaly scores that better model region-specific variations. Scores are scaled in the range  $[0, 255]$  to produce a grayscale MRAD map, where pixels with

values below a predefined threshold are classified as anomaly-free and set to zero, and remaining high-scoring pixels are retained for further analysis.

### B. Noise Removal

A major source of false positives is random amplification in black background regions, where small color variations can produce spuriously high anomaly scores that are not effectively filtered by simple thresholding. To mitigate this issue, we analyze the spatial distribution of anomaly scores within each grid cell before generating the final anomaly score map.

First, a preliminary check identifies grid cells that are likely to contain a large anomaly: if more than 90% of the scores in a cell exceed the minimum MRAD score, the entire cell is marked as anomalous. Next, a kernel-based method removes noise caused by random score variations. A sliding-window kernel (with a size  $\sim 10\%$  of the grid dimensions) is used to compute the local standard deviation of anomaly scores; regions with a standard deviation below an empirical threshold (about 3–5%) are considered to be indicative of uniform background noise and their scores are set to zero. Finally, a Gaussian blur is applied to the noise-filtered score map to smooth local fluctuations and merge fragmented anomalous regions, improving region contiguity for subsequent detection.

### C. Clustering via Region Growing

Region growing [35] is employed to cluster anomalous pixels into distinct objects based on pixel location and anomaly score. The implementation in MRAD relies on three parameters: the seed (initial pixel for expansion), the footprint (square search neighbourhood), and the tolerance (allowable score deviation for aggregation). Both the footprint and the tolerance are set empirically.

Seed pixels are found by applying mean-shift clustering [36] to the blurred score map. This non-parametric, mode-seeking algorithm detects clusters by shifting each pixel toward the region of highest density, iterating until convergence at a local maximum. The resulting cluster centroids serve as seed points for region growing.

Region growing then expands from each seed, aggregating spatially adjacent pixels with similar anomaly scores until no further candidates meet the criteria. This yields a binary anomaly map, from which the total number of anomalous pixels is computed. An image is classified as anomalous if this count exceeds a predefined threshold. The complete MRAD pipeline is outlined in Algorithm 1, with an illustrative example in Fig. 5.

## V. EXPERIMENTS

Using the ALLO benchmark, we evaluate our proposed algorithm, MRAD, against recent unsupervised anomaly detection algorithms from the industrial and medical domains. We then analyze the limitations of these competing methods and investigate the factors that contribute to the superior performance of MRAD.

### A. Experimental Setup

We modified the Intel Anomalib library [37] to load, train, and evaluate learning-based algorithms on the ALLO dataset. We selected eight representative learning-based methods from the library, chosen to cover both reconstruction- and representation-based approaches and for their established performance on the MVTEC industrial benchmark.

Normalizing flow-based methods, FastFlow [24] and UFlow [38], learn the probability distribution of normal image features and detect anomalies as samples with low likelihood. Student-teacher methods, including STFPM [25] and Reverse Distillation [21], train a smaller student network to mimic the feature representations of a pre-trained teacher, flagging deviations as anomalies. Self-supervised and reconstruction-based methods, such as DRAEM [18], DSR [19], and SuperSimpleNet [39], reconstruct normal images or leverage synthetic anomalies to train models to discriminate between normal and abnormal data. Finally, CFA [22] is a feature-adaptation method that maps normal features to a shared hypersphere, detecting anomalies as features that fail to map correctly. Representation-based methods generally use fixed encoders pre-trained on ImageNet [40], while training remaining layers from scratch on the target dataset.

---

#### Algorithm 1 Model-Reference Anomaly Detection

---

```

ScoreImage = Zeros(SizeOf(QueryImage))
AnomalyMap = Zeros(SizeOf(QueryImage))
for GridCell in QueryImage do
  for Pixel in GridCell do
    Score = MRAD(Pixel) ▷ See Eq. (2)
    if Score > MinMRADScore then
      ScoreImage[Pixel] = Score
    end if
  end for
  StdDev = StandardDeviation(GridCell, Kernel)
  if Range(StdDev) < 3% then
    Set Score = 0 for all pixels in GridCell
  end if
end for
Apply Gaussian blur to ScoreImage
Apply mean shift clustering to ScoreImage
Seeds = FindClusterCentroids(ScoreImage)
for StartPoint in Seeds do
  AnomalyMap[StartPoint] = 1 ▷ Anomalous pixel
  for Pixel in Footprint(StartPoint) do
    if InBounds(Pixel, Tolerance) then
      AnomalyMap[Pixel] = 1 ▷ Anomalous pixel
    end if
  end for
end for
Count = Sum(AnomalyMap)
if Count > AnomalyThreshold then
  ImageClass = Anomalous
else
  ImageClass = Normal
end if

```

---

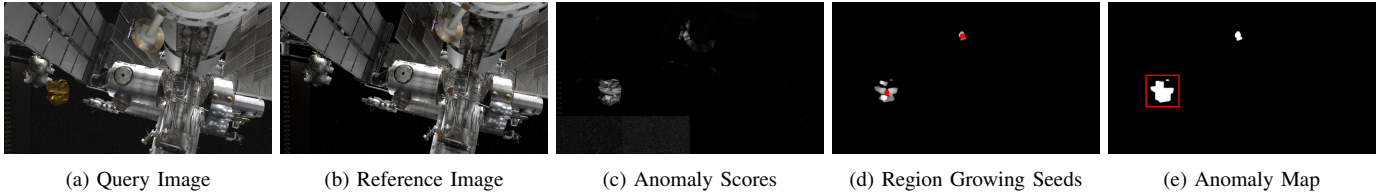


Fig. 5: Visualization of the steps in the MRAD algorithm. The query image (a) and reference image (b) are the inputs to the algorithm. The anomaly score image (c), computed using (2), highlights the anomalous thermal blanket. Noise is removed and a Gaussian blur is applied, followed by mean-shift clustering to identify region growing seed points (d). Region growing aggregates anomalous pixels to generate the final anomaly map (e), accurately detecting the blanket while rejecting false positives. Notably, camera pose variations may introduce additional image differences that could be mistaken for anomalies if detection relied solely on pixel differences alone.

The proposed MRAD and the statistical detectors RXD and PAD were also evaluated on the ALLO test set with additional rendered reference images. RXD operates solely on the query image, while PAD and MRAD use both query and reference images; their anomaly scores were thresholded to produce output binary anomaly maps.

Ablation studies were also performed on MRAD to evaluate the effect of grid size and region-growing tolerance on detection performance. Grid size and tolerance were varied above and below their optimized values to assess robustness.

Performance was evaluated via image-level AUROC (I.AUROC), pixel-level AUROC (P.AUROC), and pixel-level average precision (P.AP). For pixel-level assessment on the imbalanced ALLO dataset, P.AUROC can be inflated by the predominant negative class, potentially obscuring localization failures. P.AP, which evaluates the precision-recall balance specifically for the anomalous class, offers a more robust metric for localization accuracy in this context [23]. Consequently, P.AP was the principal metric used for performance ranking.

### B. ALLO Benchmark Results

The performance of existing learning-based algorithms on the ALLO test set, compared to their MVTec results, is summarized in Table II. Among the learning-based methods, FastFlow achieved the highest P.AP (29.1%), followed by UFlow (20.7%) and STFPM (12.5%). FastFlow also recorded the best I.AUROC (65.9%) and P.AUROC (90.4%) scores on ALLO. However, its performance dropped substantially compared to MVTec, with a 33.5% decrease in I.AUROC and an 8.1% drop in P.AUROC. Overall, normalizing flow-based methods (FastFlow and UFlow) performed best, whereas semi-supervised approaches (DRAEM and DSR) performed poorly.

The results of MRAD and other learning-free algorithms are presented in Table III. MRAD achieved the highest P.AP (62.1%) and I.AUROC (74.9%), outperforming both PAD (P.AP: 57.1%) and the best learning-based method, FastFlow (I.AUROC: 65.9%). Qualitative examples of MRAD, FastFlow, and STFPM inferences on ALLO are shown in Fig. 6.

Ablation studies highlight MRAD’s robustness to parameter variations. Increasing the grid size from its optimized value reduced P.AP by 2.9% and I.AUROC by 7.3%, whereas decreasing the region-growing tolerance caused only a 1.1% P.AP drop with no effect on I.AUROC.

### C. Discussion

1) *Limitations of Learning-Based Methods:* Analysis of our results (Section V-B) reveals the limitations of established

anomaly detection methods within the space domain. Many leverage feature extractors pre-trained on ImageNet, a dataset whose visual characteristics differ significantly from ALLO. Consequently, these networks generate non-discriminative features when applied to ALLO data, compromising their effectiveness in learning the dataset’s distribution.

Furthermore, some methods assume anomaly-free data follow a unimodal distribution [20], [24], which is problematic for datasets where anomalies closely resemble normal data or where normal data is inherently multi-modal [18]. A major limitation of existing methods is their assumption of image consistency. Many were designed for applications with fixed lighting and viewpoints (e.g., industrial defect inspection). As a result, anomaly scores can be unreliable when there are misalignments between training and test images. Normalizing flow-based methods, such as FastFlow [24] and UFlow [38], are better able to handle complex distributions, reducing false positives. However, even these top-performing algorithms struggle to detect anomalies with colors similar to the station.

Learned methods applied to the ALLO dataset struggle to detect anomalies as they attempt to model a global distribution of non-anomalous features. MRAD overcomes this by analyzing each query image individually and leveraging its corresponding anomaly-free reference image.

2) *Statistical (Learning-Free) Anomaly Detection:* Further analysis of our results demonstrates how a non-learning algorithm can be used for anomaly detection and what information can be leveraged to improve performance. The benefits of using a reference image are observed in the performance increase between RXD and PAD. By calculating background statistics from reference images rather than query images, PAD improved the P.AP of RXD by 39.5%. MRAD further builds on PAD by incorporating noise removal and region growing to reduce false positives and cluster anomalous pixels, leading to a 5% increase in P.AP and an 18.6% improvement in I.AUROC.

The impact of grid size on MRAD’s anomaly detection performance demonstrates how reference images enhance detection. Large grids consider a broader context around a query pixel but often miss fine-grained local anomalies. In contrast, smaller grids better leverage the reference image to detect local deviations. Similarly, low region-growing tolerance values encourage the grouping of nearby anomalous pixels by reinforcing local consistency in anomaly scores. However, high tolerance values tend to incorrectly include non-anomalous pixels, reducing detection accuracy.

Importantly, MRAD’s simple statistical formulation and few

TABLE II: Performance of state-of-the-art anomaly detection algorithms on the ALLO and MVTEC test sets. For each metric, the three top-performing methods are highlighted in red, orange and yellow, respectively.

Dataset	Metric	DSR [19]	Rev. Dist. [21]	SuperSimpleNet [39]	CFA [22]	DRAEM [18]	STFPM [25]	UFlow [38]	FastFlow [24]
MVTEC	I.AUROC $\uparrow$	98.2	98.5	98.0	99.5	98.0	95.5	98.9	99.4
	P.AUROC $\uparrow$	-	97.8	-	98.5	97.3	97.0	98.7	98.5
	P.AP $\uparrow$	70.2	-	-	-	68.4	-	-	-
ALLO	I.AUROC $\uparrow$	55.6 $\pm$ 2.0	57.4 $\pm$ 4.4	49.6 $\pm$ 0.5	51.3 $\pm$ 0.5	55.4 $\pm$ 1.3	61.8 $\pm$ 2.4	60.7 $\pm$ 3.2	65.9 $\pm$ 0.6
	P.AUROC $\uparrow$	69.5 $\pm$ 6.5	75.7 $\pm$ 0.7	79.5 $\pm$ 9.5	84.8 $\pm$ 7.7	77.1 $\pm$ 2.2	87.8 $\pm$ 1.7	85.8 $\pm$ 1.6	90.4 $\pm$ 0.5
	P.AP $\uparrow$	6.9 $\pm$ 0.7	7.0 $\pm$ 2.5	9.3 $\pm$ 1.0	11.0 $\pm$ 2.8	12.1 $\pm$ 1.4	12.5 $\pm$ 1.3	20.7 $\pm$ 1.6	29.1 $\pm$ 1.2

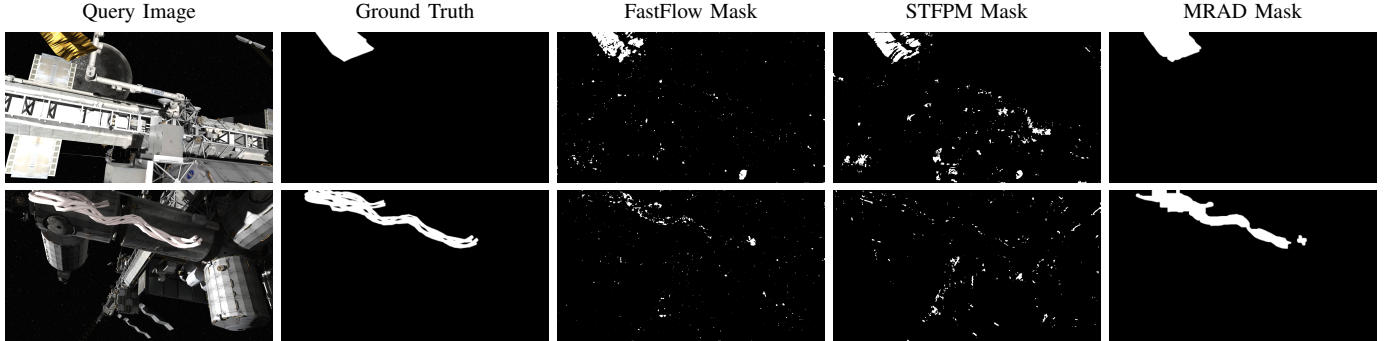


Fig. 6: Examples of predicted anomaly masks for two images from the ALLO test set by two learning-based algorithms, FastFlow and STFPM, and by MRAD. Ground truth masks are provided for comparison. *Top Row*: The anomalous object, a thermal blanket, is located in the upper left of the query image. *Bottom Row*: The anomalous object, a power cable, is located in the upper centre of the query image.

tunable parameters make it interpretable and easy to adapt across different operational scenarios. Unlike deep learning approaches, which are often black boxes that can require retraining, MRAD’s explicit use of background statistics provides predictable behavior.

Furthermore, this statistical approach circumvents the significant data dependency of deep learning. Acquiring extensive real data in orbit is prohibitively expensive, and training on synthetic data introduces a sim-to-real gap that can compromise on-orbit performance. MRAD avoids these challenges of data acquisition and domain adaptation by generating its reference image at inference time from a known CAD model and pose information. However, this reliance on a predefined model also presents limitations; because MRAD does not learn from data, its performance is limited by the quality of the reference image and the validity of the underlying statistical assumptions.

## VI. CONCLUSION

In this paper, we addressed the task of visual anomaly detection and localization for a space station in lunar orbit, a

TABLE III: Results of MRAD and other statistical anomaly detection baselines on the ALLO test set. The three top-performing methods are highlighted in red, orange and yellow, respectively.

Algorithm	I. AUROC $\uparrow$	P. AUROC $\uparrow$	P. AP $\uparrow$
RXD	50.0	55.1	17.6
PAD	56.3	70.1	57.1
MRAD (8x8 grids)	75.7	73.6	60.0
MRAD (2x2 grids)	65.6	65.1	59.2
MRAD (small tolerance)	74.9	68.3	61.0
MRAD (large tolerance)	68.5	67.3	54.9
MRAD	74.9	70.0	62.1

valuable yet unexplored area for autonomous space operations. We introduced ALLO, the first open-source anomaly detection dataset with synthetic lunar orbit imagery, and established a benchmark for the space domain by evaluating state-of-the-art methods. To overcome the limitations of existing approaches, we proposed MRAD, a novel, statistical algorithm that leverages known camera poses and a CAD model of the station to render an anomaly-free reference image and detect anomalies as statistical deviations. MRAD achieves state-of-the-art performance on the ALLO dataset, outperforming existing methods in both pixel-level AP and image-level AUROC. This work demonstrates the importance of robust anomaly detection and shows how a statistical approach can enhance the autonomy of robotic systems in space.

While MRAD achieves strong results, its reliance on accurate CAD models and runtime rendering introduces practical constraints. Learning-based methods, though potentially more computationally efficient, currently fail to generalize to the varied lighting and geometric conditions of the space domain. A promising direction for future work is to develop novel learning strategies, where models are trained to discriminate between normal and anomalous synthetic examples. By explicitly teaching a model what constitutes an anomaly in this specific domain, we could enhance its discriminative power and robustness to the extreme lighting and viewpoint variability, enabling reliable anomaly detection for future autonomous space operations.

## REFERENCES

- [1] J. C. Crusan, R. M. Smith, D. A. Craig, J. M. Caram, J. Guidi, M. Gates, J. M. Krezel, and N. B. Herrmann, “Deep space gateway concept: Extending human presence into cislunar space,” in *2018 IEEE Aerospace Conference*, March 2018, pp. 1–10. [Online]. Available: <https://ieeexplore.ieee.org/document/8396541>

- [2] (2020, June) About Canadarm3. <https://www.asc-csa.gc.ca/eng/canadarm3/about.asp>. Last updated: 2025-02-25.
- [3] Blender. <https://www.blender.org/>.
- [4] Unreal engine 5. <https://www.unrealengine.com/en-US/unreal-engine-5>.
- [5] R. Brochard, J. Lebreton, C. Robin, K. Kanani, G. Jonniaux, A. Masson, N. Despré, and A. Berjaoui, "Scientific image rendering for space scenes with the SurRender software," in *International Astronautical Conference 2018*, Bremen, Germany, 2018.
- [6] M. Pajusalu, I. Iakubivskiy, G. J. Schwarzkopf, O. Knuutila, T. Väisänen, M. Bühner, H. Teras, G. L. Bonhomme, M. F. Palos, J. Praks, and A. Slavinskis, "SISPO: Space imaging simulator for proximity operations," *PLOS ONE*, vol. 17, no. 3, p. e0263882, March 2022. [Online]. Available: <https://journals.plos.org/plosone/article?id=10.1371/journal.pone.0263882>
- [7] C. L. Gentil, J. Naylor, N. Munasinghe, J. Mehmi, B. Dai, M. Asavkin, D. G. Dansereau, and T. Vidal-Calleja, "Mixing data-driven and geometric models for satellite docking port state estimation using an RGB or event camera," in *International Conference on Robotics and Automation (ICRA)*, 2025.
- [8] P. Bergmann, M. Fausser, D. Sattlegger, and C. Steger, "MVTec AD—A comprehensive real-world dataset for unsupervised anomaly detection," in *2019 IEEE/CVF Conference on Computer Vision and Pattern Recognition (CVPR)*, 2019, pp. 9584–9592. [Online]. Available: <https://ieeexplore.ieee.org/document/8954181>
- [9] Y. Zheng, X. Wang, Y. Qi, W. Li, and L. Wu, "Benchmarking unsupervised anomaly detection and localization," *arXiv preprint arXiv:2205.14852*, 2022. [Online]. Available: <https://arxiv.org/abs/2205.14852>
- [10] MyNew, "Btech dataset," <https://universe.roboflow.com/mynew/btech>, feb 2024, visited on 2024-09-11. [Online]. Available: <https://universe.roboflow.com/mynew/btech>
- [11] D. Tabernik, S. Šela, J. Skvarč, and D. Škočaj, "Segmentation-Based Deep-Learning Approach for Surface-Defect Detection," *Journal of Intelligent Manufacturing*, May 2019.
- [12] L. Ruff, J. R. Kauffmann, R. A. Vandermeulen, G. Montavon, W. Samek, M. Kloft, T. G. Dietterich, and K.-R. Müller, "A unifying review of deep and shallow anomaly detection," *Proceedings of the IEEE*, vol. 109, no. 5, pp. 756–795, May 2021. [Online]. Available: <https://ieeexplore.ieee.org/document/9347460/?arnumber=9347460>
- [13] L. M. Manevitz and M. Yousef, "One-class SVMs for document classification," *Journal of Machine Learning Research*, vol. 2, pp. 139–154, 2001. [Online]. Available: <https://jmlr.csail.mit.edu/papers/v2/manevitz01a.html>
- [14] H. Hoffmann, "Kernel PCA for novelty detection," *Pattern Recognition*, vol. 40, no. 3, pp. 863–874, March 2007. [Online]. Available: <https://www.sciencedirect.com/science/article/pii/S0031320306003414>
- [15] I. Reed and X. Yu, "Adaptive multiple-band CFAR detection of an optical pattern with unknown spectral distribution," *IEEE Transactions on Acoustics, Speech, and Signal Processing*, vol. 38, no. 10, pp. 1760–1770, 1990. [Online]. Available: <https://ieeexplore.ieee.org/document/60107>
- [16] L. Gao, Q. Guo, A. J. Plaza, J. Li, and B. Zhang, "Probabilistic anomaly detector for remotely sensed hyperspectral data," *Journal of Applied Remote Sensing*, vol. 8, no. 1, p. 083538, November 2014. [Online]. Available: <https://www.spiedigitallibrary.org/journals/journal-of-applied-remote-sensing/volume-8/issue-1/083538/Probabilistic-anomaly-detector-for-remotely-sensed-hyperspectral-data/10.1117/1.JRS.8.083538.full>
- [17] B. Du and L. Zhang, "Random-selection-based anomaly detector for hyperspectral imagery," *IEEE Transactions on Geoscience and Remote Sensing*, vol. 49, no. 5, pp. 1578–1589, May 2011. [Online]. Available: <https://ieeexplore.ieee.org/document/5628269>
- [18] V. Zavrtnik, M. Kristan, and D. Škočaj, "DR<sub>EM</sub>—A discriminatively trained reconstruction embedding for surface anomaly detection," *2021 IEEE/CVF International Conference on Computer Vision*, pp. 8310–8319, October 2021. [Online]. Available: <https://ieeexplore.ieee.org/document/9710329/>
- [19] V. Zavrtnik, M. Kristan, and D. Škočaj, "DSR—A dual subspace reconstruction network for surface anomaly detection," in *Computer Vision – ECCV 2022*, ser. Lecture Notes in Computer Science, S. Avidan, G. Brostow, M. Cissé, G. M. Farinella, and T. Hassner, Eds. Springer Nature Switzerland, 2022, pp. 539–554.
- [20] T. Defard, A. Setkov, A. Loesch, and R. Audigier, "PaDiM: A patch distribution modeling framework for anomaly detection and localization," in *Pattern Recognition. ICPR International Workshops and Challenges: Virtual Event, January 10–15, 2021, Proceedings, Part IV*. Springer-Verlag, January 2021, pp. 475–489. [Online]. Available: [https://doi.org/10.1007/978-3-030-68799-1\\_35](https://doi.org/10.1007/978-3-030-68799-1_35)
- [21] H. Deng and X. Li, "Anomaly detection via reverse distillation from one-class embedding," in *2022 IEEE/CVF Conference on Computer Vision and Pattern Recognition (CVPR)*. IEEE, June 2022, pp. 9727–9736. [Online]. Available: <https://ieeexplore.ieee.org/document/9879956/>
- [22] S. Lee, S. Lee, and B. C. Song, "CFA: Coupled-hypersphere-based feature adaptation for target-oriented anomaly localization," *IEEE Access*, vol. 10, pp. 78 446–78 454, 2022. [Online]. Available: <https://ieeexplore.ieee.org/document/9839549/?arnumber=9839549>
- [23] D. Gudovskiy, S. Ishizaka, and K. Kozuka, "CFLOW-AD: Real-time unsupervised anomaly detection with localization via conditional normalizing flows," in *2022 IEEE/CVF Winter Conference on Applications of Computer Vision*, January 2022, pp. 1819–1828. [Online]. Available: <https://ieeexplore.ieee.org/document/9707081/?arnumber=9707081>
- [24] J. Yu, Y. Zheng, X. Wang, W. Li, Y. Wu, R. Zhao, and L. Wu, "FastFlow: Unsupervised anomaly detection and localization via 2D normalizing flows," *arXiv preprint arXiv:2111.07677*, 2021. [Online]. Available: <http://arxiv.org/abs/2111.07677>
- [25] G. Wang, S. Han, E. Ding, and D. Huang, "Student-teacher feature pyramid matching for anomaly detection," in *British Machine Vision Conference*, March 2021. [Online]. Available: <https://www.semanticscholar.org/paper/Student-Teacher-Feature-Pyramid-Matching-for-Wang-Han/02805f18989b7e77f30ee13defd6fecfd0f499f>
- [26] International space station 3d model - NASA science. <https://science.nasa.gov/resource/international-space-station-3d-model/>.
- [27] D. E. Lee, "White paper: Gateway destination orbit model: A continuous 15 year NRHO reference trajectory," NTRS Author Affiliations: NASA Johnson Space Center NTRS Report/Patent Number: JSC-E-DAA-TN72594 NTRS Document ID: 20190030294 NTRS Research Center: Johnson Space Center (JSC). [Online]. Available: <https://ntrs.nasa.gov/citations/20190030294>
- [28] B. Rhodes, "Skyfield: High precision research-grade positions for planets and Earth satellites generator," Astrophysics Source Code Library, record ascl:1907.024, Jul. 2019.
- [29] R. Zhang, P. Isola, A. A. Efros, E. Shechtman, and O. Wang, "The unreasonable effectiveness of deep features as a perceptual metric," in *Proceedings of the IEEE Conference on Computer Vision and Pattern Recognition*, 2018, pp. 586–595. [Online]. Available: [https://openaccess.thecvf.com/content\\_cvpr\\_2018/html/Zhang\\_The\\_Unreasonable\\_Effectiveness\\_CVPR\\_2018\\_paper.html](https://openaccess.thecvf.com/content_cvpr_2018/html/Zhang_The_Unreasonable_Effectiveness_CVPR_2018_paper.html)
- [30] J. Y. Koh, D. Fried, and R. R. Salakhutdinov, "Generating images with multimodal language models," *Advances in Neural Information Processing Systems*, vol. 36, pp. 21 487–21 506, 2023. [Online]. Available: [https://proceedings.neurips.cc/paper\\_files/paper/2023/hash/43a69d143273bd8215578bde887bb552-Abstract-Conference.html](https://proceedings.neurips.cc/paper_files/paper/2023/hash/43a69d143273bd8215578bde887bb552-Abstract-Conference.html)
- [31] D. Podell, Z. English, K. Lacey, A. Blattmann, T. Dockhorn, J. Müller, J. Penna, and R. Rombach, "SDXL: Improving latent diffusion models for high-resolution image synthesis," in *The Twelfth International Conference on Learning Representations*, 2023. [Online]. Available: <https://openreview.net/forum?id=di52zR8xgf>
- [32] M. Heusel, H. Ramsauer, T. Unterthiner, B. Nessler, and S. Hochreiter, "Gans trained by a two time-scale update rule converge to a local nash equilibrium," *Advances in neural information processing systems*, vol. 30, 2017.
- [33] Y. Zhu, B. Li, H. Zhang, X. Li, L. Xu, and L. Bing, "Stabilize the latent space for image autoregressive modeling: A unified perspective," *Advances in Neural Information Processing Systems*, vol. 37, pp. 28 636–28 661, 2024.
- [34] S. Lee, M. Kim, Y. Chae, and B. Stenger, "Linearly controllable gan: Unsupervised feature categorization and decomposition for image generation and manipulation," in *European Conference on Computer Vision*. Springer, 2024, pp. 229–245.
- [35] R. Adams and L. Bischof, "Seeded region growing," *IEEE Transactions on Pattern Analysis and Machine Intelligence*, vol. 16, no. 6, pp. 641–647, 1994, conference Name: IEEE Transactions on Pattern Analysis and Machine Intelligence. [Online]. Available: <https://ieeexplore.ieee.org/abstract/document/295913>
- [36] Y. Cheng, "Mean shift, mode seeking, and clustering," *IEEE Transactions on Pattern Analysis and Machine Intelligence*, vol. 17, no. 8, pp. 790–799, 1995. [Online]. Available: <https://ieeexplore.ieee.org/document/400568>
- [37] S. Akcay, D. Ameln, A. Vaidya, B. Lakshmanan, N. Ahuja, and U. Genc, "Anomalib: A deep learning library for anomaly detection," in *2022 IEEE International Conference on Image Processing*, October 2022, pp. 1706–1710. [Online]. Available: <https://ieeexplore.ieee.org/abstract/document/9897283>

- [38] M. Tailanian, A. Pardo, and P. Muse, "U-flow: A u-shaped normalizing flow for anomaly detection with unsupervised threshold," *Journal of Mathematical Imaging and Vision*, vol. 66, no. 4, pp. 678–696, August 2024. [Online]. Available: <https://doi.org/10.1007/s10851-024-01193-y>
- [39] B. Rolih, M. Fučka, and D. Skočaj, "SuperSimpleNet: Unifying unsupervised and supervised learning for fast and reliable surface defect detection," in *International Conference on Pattern Recognition*. Springer, 2025, pp. 47–65.
- [40] A. Krizhevsky, I. Sutskever, and G. E. Hinton, "ImageNet classification with deep convolutional neural networks," in *Advances in Neural Information Processing Systems*, vol. 25. Curran Associates, Inc., 2012. [Online]. Available: <https://proceedings.neurips.cc/paper/2012/hash/c399862d3b9d6b76c8436e924a68c45b-Abstract.html>